Nuclear Engineering and Technology 57 (2025) 103335

Contents lists available at ScienceDirect

Nuclear Engineering and Technology

journal homepage: www.elsevier.com/locate/net

Original Article

Insights and simulation of metascintillator-based brain PET systems to enhance ToF capability

D.A.B. Bonifacio [a,b,*], R. Latella [b], H.M. Murata [c,d], J.M. Benlloch [b], A.J. Gonzalez [b], P. Lecoq [e], G. Konstantinou [e]

[a] *Nuclear and Energy Research Institute, IPEN/CNEN, Brazil*
[b] *Instituto de Instrumentación para Imagen Molecular, I3M/UPV/CSIC, Spain*
[c] *Institute of Radioprotection and Dosimetry, IRD/CNEN, Brazil*
[d] *Gaugit, Brazil*
[e] *Metacrystal SA, Switzerland*

ARTICLE INFO

Keywords:
Positron emission tomography
Metascintillators
Heterostructures
Time of flight
Monte Carlo simulation

ABSTRACT

The integration of Time-of-Flight (ToF) information into Positron Emission Tomography (PET) image reconstruction enhances both signal-to-noise ratio and the localization of annihilation events. A critical component contributing to the accuracy of ToF-PET is the scintillator. To overcome the time resolution limitations in conventional scintillators, the metascintillator approach has been proposed. The metascintillator is an engineered composition of small units that combines and optimizes various features within a single scintillator heterostructure.

In this work, metascintillator-based brain PET systems were simulated using the GATE toolkit and compared with designs based on bulk LYSO or BGO. Sensitivity, noise equivalent count rate (NECR) and scatter fraction were evaluated following NEMA guidelines. To match the peak sensitivity of a system utilizing a 15 mm bulk BGO, the metascintillator-based scanners using BGO/BaF_2, BGO/EJ232, LYSO/BaF_2 and LYSO/EJ232 must possess thicknesses of 23.2 mm, 22.5 mm, 29.7 mm and 31.1 mm, respectively. With ToF gain, the scanner utilizing a 25 mm thick LYSO-EJ232 metascintillator exhibited the most promising NECR curve, peaking at 1180 cps at 1600 MBq. This work takes a significant step towards harnessing the information gain facilitated by the integration of metascintillator-based detectors in PET imaging.

1. Introduction

Positron Emission Tomography (PET) plays a pivotal role in tumor imaging and the search for metastases [1]. There are several ongoing investigations for the development of brain-dedicated PET systems [2–9] for the diagnosis of diseases associated with various forms of dementia. The reduced ring diameter of a brain-dedicated PET scanner compared to whole-body PET systems enhances spatial resolution by mitigating the non-collinearity effect of positron annihilation and increases sensitivity through improved solid angle coverage.

Advancements in PET technology have markedly improved performance, driven by significant progress in instrumentation and software. Recent trends incorporate time-of-flight (ToF) information into the image reconstruction process to enhance signal-to-noise ratio (SNR) and annihilation event localization [10]. Among the crucial components contributing to the accuracy of ToF-PET is the scintillation crystal. The evolution of scintillation crystals is evidenced by the emergence of inorganic scintillators boasting superior energy resolution, faster response and heightened detection efficiency [11]. Traditionally, scintillator development revolves around the discovery of novel materials and the enhancement of existing ones [12]. These materials typically possess a homogeneous chemical composition and structure without any secondary phase. Notably, BGO crystal (e.g. GE Omni Legend) and lutetium-based scintillators – LSO, LYSO and LFS – (e.g. Siemens Biograph Vision) have found widespread application [13]. Despite the prevalent use of LYSO, various studies are exploiting Cherenkov emission by introducing ToF in BGO [14–30]. Previous studies also proposed the use of $LaBr_3$:Ce crystal [31] and plastic scintillator [32] to develop PET systems with ToF capabilities. More recently, the metascintillator approach has emerged to address the time resolution limitations of conventional scintillators [33]. Subsequently, numerous works have explored its potential [34–37]. The metascintillator is an engineered composition of units with at least one dimension in the order of 100 μm, amalgamating and optimizing multiple features within a single

---

[*] Corresponding author at: Nuclear and Energy Research Institute, IPEN/CNEN, Brazil.
E-mail addresses: daniel.bonifacio@ird.gov.br, daniel.bonifacio@ipen.br (D.A.B. Bonifacio).

https://doi.org/10.1016/j.net.2024.11.037
Received 2 July 2024; Received in revised form 21 October 2024; Accepted 21 November 2024

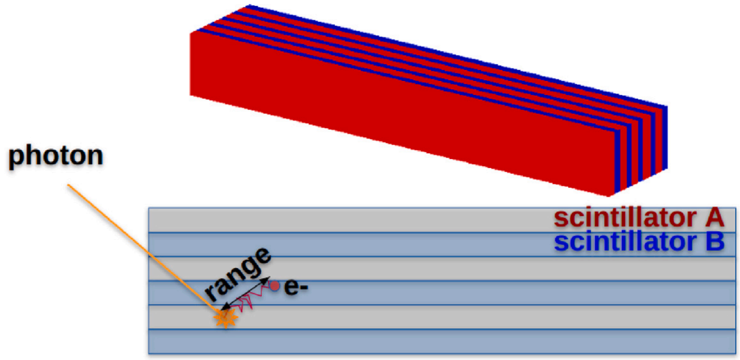

Fig. 1. (Top) Metascintillator configuration in a pixel structure, using two different materials; and (bottom) representation of the recoil electron interacting with a metascintillator along its range.

scintillator heterostructure (see Fig. 1). When incident radiation interacts with the metascintillator, a recoil electron is formed, gradually losing energy along its path. The scintillator heterostructure follows a probability distribution to share the energy of the radiation interaction among different materials and combine their properties. Thus, scintillator heterostructure has to be designed considering the range of the recoil electron, which is typically 100 to 200 μm in BGO and LYSO crystals [38].

Monte Carlo simulation is frequently employed for assessing the performance of medical imaging devices in emission tomography, optimizing acquisition protocols, and refining image reconstruction algorithms and correction techniques [39,40]. GATE (Geant4 Application for Emission Tomography) [41] radiation transport code, based on Geant4 toolkit [42], was specifically developed to facilitate those tasks, encompassing time-dependent processes, acquisition, and signal processing stages for comprehensive system simulation.

A previous study proposed a metascintillator-based TOF-PET geometry employing BGO and plastic EJ232 scintillators for image reconstruction analysis using simulated data [43]. Building upon this, the current work simulates brain PET systems based on metascintillator technology using GATE and compares them with designs relying on bulk LYSO or BGO. Several metascintillator thicknesses were simulated to ascertain their equivalence to a 15 mm thick bulk BGO crystal in terms of sensitivity. Additionally, the noise equivalent count rate (NECR) and scatter fraction (SF) were assessed adhering to the guidelines outlined by the National Electrical Manufacturers Association (NEMA) [44]. To ensure a fair comparison and avoid bias introduced by specific image reconstruction algorithms, only data in the list-mode format (i.e., event-by-event recorded information) were utilized for analysis. The primary objective of this study is to take a significant step towards realizing the clinical benefits, particularly in terms of information gain, offered by the integration of metascintillator-based detectors in PET imaging [34].

2. Materials and methods

2.1. GATE script development

GATE scripts were implemented to simulate brain-dedicated PET systems using bulk crystals and metascintillators. The simulated PET scanner evaluation tests are independent of image reconstruction and comprised sensitivity, NECR and SF. In the absence of a specific NEMA standard for brain PET systems, the analysis was performed using NEMA standards for preclinical (NEMA NU 4-2008) [44] and clinical PET systems (NU 2-2018) [45]. Simulations included 72 PET listmode acquisitions for the scatter phantom (NECR and SF curves) and 528 for the sensitivity analysis. Simulations were performed on a PC based on the Intel© Core™ i7-11700 @ 2.50 GHz (8 cores) and 32 GB RAM.

Table 1
Materials properties.

Material	ρ (g/cm^3)	LY (ph/keV)	Decay time (ns)	Ref.	λ (cm)
LYSO	7.1	33	36	[47]	1.29
BGO	7.1	8.5	300	[48]	1.10
BaF$_2$ (fast)	4.88	1.4	0.7	[48]	2.29
BaF$_2$ (slow)	4.88	9.5	620	[48]	2.29
EJ232	1.023	8.4	1.6	[49]	10.47

Table 2
LYSO material composition.

Element	Z	Mass fraction
Lu	71	0.71446
O	8	0.18148
Si	14	0.06372
Y	39	0.04034

2.2. PET geometry and materials

Geometry tests were conducted using the command "/geometry/test/run" to verify and prevent overlapping regions. The PET geometry has six rings with 290 mm transaxial diameter and 28.2 mm axial extension each one. The rings have a 1.2 mm separation between them, resulting in a total axial extension of 175.2 mm. Fig. 2 shows the PET geometry at different angular views. The dimensions were chosen for suitable brain PET imaging [46].

Each detector ring contains 30 modules of 8 × 8 crystal elements with a pitch of 3.6 mm in both directions. The pitch size was chosen to be larger than the scintillator pixel size to account for photosensor matrix spacing and the dead area between the scintillators due to reflectors and mechanical stability of the material. The materials considered for the crystal elements are described in Table 1. The mass density (ρ), the light yield (LY), and the decay time were obtained from the literature [47–49]. Attenuation length (λ) at 511 keV was determined using NIST XCOM Database [50] by considering both photoelectric absorption and Compton scattering. LYSO crystal composition is described in Table 2.

Table 3 exhibits the dimensions of the simulated crystal elements. When applicable, the metascintillator configuration is also described. The pixel size values were slightly different (e.g. 2.9 mm instead of 3 mm) depending on the relevant size of the layers composing the metascintillator pixel. The thickness of such layers has an error margin closer to 5%. Thus, we considered a 3% difference in nominal values to be negligible.

The layers of the metascintillator elements are alternately placed for each different material, as can be seen in Fig. 3. BGO, BaF$_2$ and

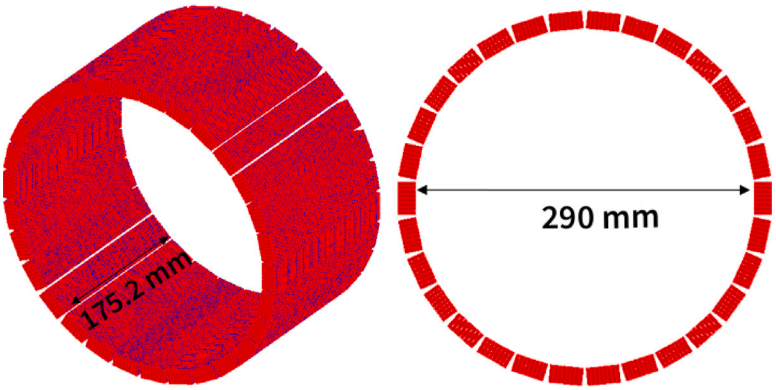

Fig. 2. Different views of the PET detector geometry.

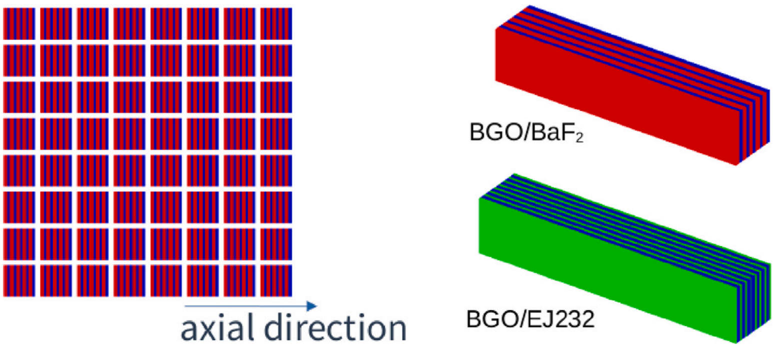

Fig. 3. Representation of the BGO/BaF$_2$ and BGO/EJ232 metascintillator elements and detailed view of the module. BGO, BaF$_2$ and EJ232 layers are represented in blue, red and green colors, respectively. (For interpretation of the references to color in this figure legend, the reader is referred to the web version of this article.)

Table 3
Dimensions of the simulated crystal elements.

Scintillator	Pixel area (mm^2)	Length (mm)	Metascintillator configuration
LYSO (Bulk)	3 × 3	20	not applicable
BGO (Bulk)	3 × 3	15	not applicable
BGO/BaF$_2$	3 × 3	15;20;25	5 × 300 μm BGO 5 × 300 μm BaF$_2$
BGO/EJ232	3 × 2.9	15;20;25	7 × 300 μm BGO 8 × 100 μm EJ232
LYSO/BaF$_2$	3 × 3	25;30;35	5 × 300 μm LYSO 5 × 300 μm BaF$_2$
LYSO/EJ232	3 × 2.9	25;30;35	7 × 300 μm LYSO 8 × 100 μm EJ232

EJ232 layers are represented in blue, red and green colors, respectively. Fig. 3 also shows the geometry of the module with the metascintillator elements.

A previous work [34] showed that not all events interact in both materials, as the average attenuation length of hot electrons in 300 μm of BGO and LYSO does nor guarantee their leakage to the fast components (EJ232 or BaF2) for all the events. However, thinner pieces of BGO and LYSO are difficult to produce or manage without significant material losses. In this sense, the thickness chosen for the different components is a compromise between performance, stability and overall sensitivity. There is just a thin air gap between layers, with no other optical coupling material applied. This configuration aims to keep a larger fraction of the scintillation light inside the layer where they are generated through the total internal reflection mechanism, which occurs when the incident angle of the optical photon is greater than the critical angle. This improves the light collection on the SiPM attached to this pixel, and therefore the timing resolution [51].

2.3. GATE parameters

Simulations were performed using GATE version 9.2 [39], which is based on Geant4 version 11.0.1 [42].

2.3.1. Physics

The Geant4 electromagnetic physics constructor “G4EmLivermore PolarizedPhysics” was chosen due to its combination of models for each physics process that offers good CPU efficiency and agreement with the reference data in medical physics applications [52–54]. This physics constructor comprises the following processes: photoelectric effect, Compton scattering, gamma conversion, Rayleigh scattering, electron and positron ionization, bremsstrahlung and multiple scattering and positron annihilation. The Geant4 radioactive decay process was also added to simulate radionuclide sources. In Geant4, secondary particles are only generated when the interacting particle has an expected range larger than a production cut, which is set in terms of a distance value. Range production cuts for gamma and electrons were set to 0.01 mm for both bulk crystals and metascintillators due to their layers with thickness values between 300 μm and 100 μm. No variance reduction technique was employed and output data were recorded and analyzed within the ROOT framework [55].

2.3.2. Digitizer

In Fig. 4, the GATE digitizer chain adopted in this work is presented. Unless otherwise specified in Table 4, the parameters employed had the default digitizer values.

The function “adder” was used to sum all the energy values from the hits that occur within the same detector module, forming a pulse. By default, GATE simulations use energy-weighted centroid positioning in the pixels of a block, similar to Anger logic. However, in this work, the policy “TakeEnergyWinner” was chosen to represent a one-to-one photosensor-crystal coupling readout. Additionally, the time of the first

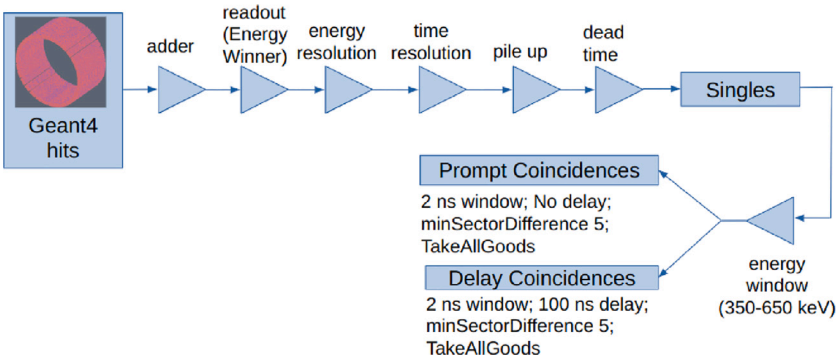

Fig. 4. GATE digitizer chain used in the simulations. The noise feature was not activated.

Table 4
Detector characteristics used in the simulations.

Scintillator	Length (mm)	ER	CTR (ps)	Dead time and pile up (ns)
LYSO	20	11%	210*	590
BGO	15	18.5%	600*	1390
	15		240*	
BGO/BaF$_2$	20	22%	244	2160
	25		249	
	15		205*	
BGO/EJ232	20	21%	210	1390
	25		216	
	25		100*	
LYSO/BaF$_2$	30	14%	114	2160
	35		129	
	25		100*	
LYSO/EJ232	30	13%	114	590
	35		129	

interaction is recorded to exclude any other contributions to timing deterioration, apart from those defined by our measurements.

Table 4 exhibits the detector characteristics used in the simulations. The energy resolution (ER) values at 511 keV, set to all singles events with and without shared energy, were obtained from a previous work [35,51,56]. The energy resolution dependence on the crystal length was not considered. The time delay distributions were considered to follow a Gaussian shape for simplicity and comparability reasons, as predefined in GATE code. However, a previous work provides measured ToF distributions with non-Gaussian shape [22]. The LYSO CTR (Coincidence Time Resolution) value refers to the state-of-the-art Siemens Biograph Vision [57]. CTR values indicated with “*” were obtained experimentally [51]. Assuming identical detectors, the CTR values in the other cases were calculated considering the timing resolution deterioration due to the contribution of the crystal length [58].

Dead time and pile up for the scintillators were set according to the pulse duration obtained from our basic experimental setup [51] and considered the slowest decay time of each material component, as described in Table 4.

The energy window for event selection was 350 keV to 650 keV for all crystal elements configurations described on Table 3. The energy window applied is based on the typical values used in PET scanners and is sufficient to register most of the events of the photopeak for all energy resolution values set in the simulations. Hence, the energy window used was based on common practice and characterization approaches. As the majority of events is predominantly releasing energy in the heavy materials, with scatter being followed by secondary photoelectric absorption, we consider the bias to be small. Therefore, scattered events (e.g. Compton scattering in one crystal and photoelectric absorption in another one) may also be registered.

The coincidence time window was set to 2 ns [59,60]. The chosen coincidence sorter is based on a “multiple-window” approach, where each registered single event triggers the opening of a time window and a logical OR records the coincidence events. This approach, used in the validation of PET scanners [40,61], avoids counting some coincidences twice [40] and is activated by setting the flag “allPulseOpenCoincGate” as true. The multiple coincidences policy “takeAllGoods” was selected to store all valid coincidences when three or more singles are found within the same coincidence window. This strategy best represents the design implemented in modern PET systems [57]. A pair of singles in coincidence is considered valid when they are separated by a minimum number of modules, defined by the parameter “minSectorDifference” of the GATE coincidence sorter. This parameter helps reject coincidence events formed by an annihilation photon that scatters and deposits its energy in adjacent blocks. In this work, the parameter “minSectorDifference” is set to 5 modules (or sectors). Estimation of the number of random counts was performed through a second coincidence module with the same time window, but with a delay of 100 ns. The same coincidence sorter and multiple coincidence policy were applied to provide a better estimation of random counts [62].

2.4. Data acquisition and analysis

2.4.1. Sensitivity

The effective sensitivity S (in %) of the scanner is defined as the ratio of the true coincidence event rate R_{true} (in counts/s) to the total activity of the source A_s (in Bq):

$$S = \frac{R_{true}}{A_s \times BF} \times 100 \quad (1)$$

The fraction of total decays that correspond to the emission of positrons (BF), also called the positron branching ratio, should be considered when dealing with non-pure beta plus emitters. For example, ^{22}Na and ^{18}F emit beta-plus particles with BF of 0.9 and 0.97, respectively [1].

The sensitivity is determined by data acquired from a uniform activity volume across all projections. During a sensitivity measurement, a sufficient amount of material must surround the source to ensure the occurrence of the annihilation process. The sensitivity is mainly determined by the geometry of the scanner and the absorption efficiency of the detector. For ToF-capable PET systems, the CTR is an important factor for the effective sensitivity since the likelihood of the annihilation’s position along the LOR is restricted by the detection time difference between the two annihilation photons. Alongside geometry and absorption efficiency, the system’s maximum and minimum energy limits, as well as its dead time, are crucial factors.

In this work, a 370 kBq ^{22}Na spherical source with 0.25 mm diameter encapsulated in a 10 mm×10 mm×10 mm^3 cast acrylic cube was used to determine sensitivity values for 40 s acquisitions at several positions across the axial direction (−75mm; −60 mm; −45 mm; −30 mm; −15 mm; 0 mm; 15 mm; 30 mm; 45 mm; 60 mm; 75 mm). This definition of the source follows the NEMA NU-4 2008 standard [44].

The length of the metascintillator-based pixel, also called metapixel, could be approximately determined by the composed attenuation length and photofraction values. However, due to the non-homogeneous and asymmetric nature of the metapixel, a more precise model is necessary for an accurate study of information gain. Furthermore, simulating the detection efficiency of a 511 keV gamma arriving normal to the entrance surface in the middle of the pixel may not accurately represent efficiency in a real PET geometry, where gammas impinge from various angles. It is also anticipated that the equivalent length of the metapixel is PET-geometry dependent, to some extent. Therefore, sensitivity profiles of each simulated brain-dedicated PET geometry were utilized to ascertain the length of metapixel configurations that exhibit performance equivalent to a $3\,\text{mm} \times 3\,\text{mm} \times 15\,\text{mm}^3$ BGO pixel.

2.4.2. NECR and SF

The NECR and SF studies were conducted according to the methodology described in a previous work [40], which reports maximum relative differences between simulated and experimental values of less than 11% for all event rates, including NECR and SF. This margin of difference is considered acceptable for our study, as it focuses on the comparative analysis of various scintillator configurations.

A true coincidence event occurs when the two annihilation photons are detected within the coincidence time window, and neither photon interacts before detection. A scattered coincidence occurs when at least one of the annihilation photons is scattered prior to detection, which implies a high probability of a wrongly assigned LOR. A random coincidence is formed when two photons from different annihilation events are registered within the same coincidence time window. Therefore, only the true coincidence events provide correct information on the spatial distribution of the radiopharmaceutical within the patient. The total count rate of detected coincidences is defined as:

$$C = T + S + R \tag{2}$$

where T, S and R are the true, scattered and random coincidence count rates, respectively. The SF should be determined by choosing the source activity in which the number of random coincidences is negligible. It is given by:

$$SF = \frac{S}{T + S} \tag{3}$$

The NECR estimates the number of true coincidences during an acquisition:

$$SNR^2 \propto NECR = \frac{T}{1 + \frac{S}{T} + \frac{R}{T}} = \frac{T^2}{T + S + R} = \frac{T^2}{C} \tag{4}$$

An accurate measure of the true coincidence events must consider the intrinsic radioactivity of the detector, as is the case with scintillators that have lutetium in their composition [63].

It is widely accepted that ToF information provides the following gain in the SNR for a given object with diameter D [64]:

$$Gain(SNR_{ToF}) = \frac{SNR_{ToF}}{SNR_{non-ToF}} = \sqrt{\alpha^2 \frac{2 \times D}{c \times CTR}} \tag{5}$$

where α^2=1/1.47 [64,65] and c is the speed of the light in the vacuum. From Eqs. (4) and (5), we conclude that the NECR gain by using ToF is given by:

$$Gain(NECR_{ToF}) = \frac{NECR_{ToF}}{NECR_{non-ToF}} = Gain(SNR_{ToF})^2 \tag{6}$$

For the NECR analysis, NEMA NU2-2018 guidelines [45] indicate the use of a scatter phantom as a polyethylene cylinder with 203 mm outside diameter and 700 mm axial extension. In this work, a ^{18}F source with 3.2 mm diameter and 700 mm axial extension was placed at a 45 mm radial distance from the axial center. The source activity ranged from 10 to 3000 MBq. As we have extracted the counts directly from the simulated data, we did not take into consideration any influence of the parallax error or other spatial resolution deterioration due to the different crystal lengths in the NECR computation. However, improvements in image quality due depth-of-interaction (DOI) information cannot be determined with the NECR analysis [66].

Table 5
Metascintillator thickness equivalent to a bulk BGO with 15 mm thickness.

Metascintillator	Sensitivity	Equivalent thickness (mm)
BGO/BaF$_2$	mean	23.2
	peak	23.7
BGO/EJ232	mean	22.5
	peak	22.7
LYSO/BaF$_2$	mean	29.7
	peak	31.1
LYSO/EJ232	mean	31.1
	peak	32.3

3. Results

3.1. Sensitivity analysis

Figs. 5 shows the sensitivity profiles for ^{22}Na with and without energy window applied. The use of the ^{22}Na point source follows the NEMA guidelines and allows the sensitivity profiles to be obtained experimentally.

Sensitivity profiles simulated with GATE were previously compared to an analytical approach from another study [67]. This study also indicates that the 1275 keV gamma from ^{22}Na decay can partially pass through the EW, thereby increasing sensitivity by as much as 13.3%.

When the energy window is not applied, the peak sensitivity values for BaF$_2$-based metascintillators are higher than those employing EJ-232, when considering the same thickness. This is due to higher probability of interaction of the BaF$_2$-based metascintillators. On the other hand, the peak sensitivity for EJ232-based metascintillators are higher than BaF$_2$-based ones when the energy window is applied. This is because of the higher photoelectric absorption provided by the BGO-EJ232 and LYSO-EJ232 configurations.

With the 350–650 keV energy window, bulk BGO and LYSO crystals provide sensitivity profiles with peak values of 8.8% and 8.5%, respectively.

It can be seen that 20 mm thick BGO/BaF$_2$ and 25 mm thick LYSO/BaF$_2$ present the lowest sensitivity profiles among the BaF$_2$-based metascintillators with a peak sensitivity of 7%. The highest sensitivity profile is obtained with a 35 mm thick LYSO/BaF$_2$ with a peak sensitivity of 10%.

Concerning sensitivity profiles with EJ232-based metascintillators, 25 mm thick LYSO/EJ232 heterostructure provides the lowest sensitivity profile with a peak sensitivity of 6.5%. The highest sensitivity profiles use the metascintillators LYSO/EJ232 and BGO/EJ232 with thicknesses of 35 mm and 25 mm, respectively. Their peak sensitivity is around 9.5%.

Figs. 6 show the relation between the sensitivity and the metascintillator thickness for a 350–650 keV energy window considering LYSO and BGO-based metascintillators. Although a linear behavior is observed for both mean and peak sensitivity values, it is known that this would not occur for a longer range of thickness values [68].

The use of BaF$_2$ with LYSO-based metascintillators provides better sensitivity than the adoption of EJ232. On the other hand, EJ232 is a better option to achieve optimal sensitivity with BGO-based metascintillators. This effect is due to the larger photoelectric absorption probability of BGO.

Table 5 shows the values of metascintillator thickness to match the peak sensitivity of a PET system based on a bulk BGO with a thickness of 15 mm. These values were obtained through a linear fitting procedure using data presented in Fig. 6.

The metascintillator thicknesses for the mean and peak sensitivity differs from only 0.2 mm for the BGO/EJ232 to 1.4 mm for the LYSO/BaF$_2$. The higher the probability of photoelectric absorption in the materials, the lower the difference of thickness values for the mean and peak sensitivity.

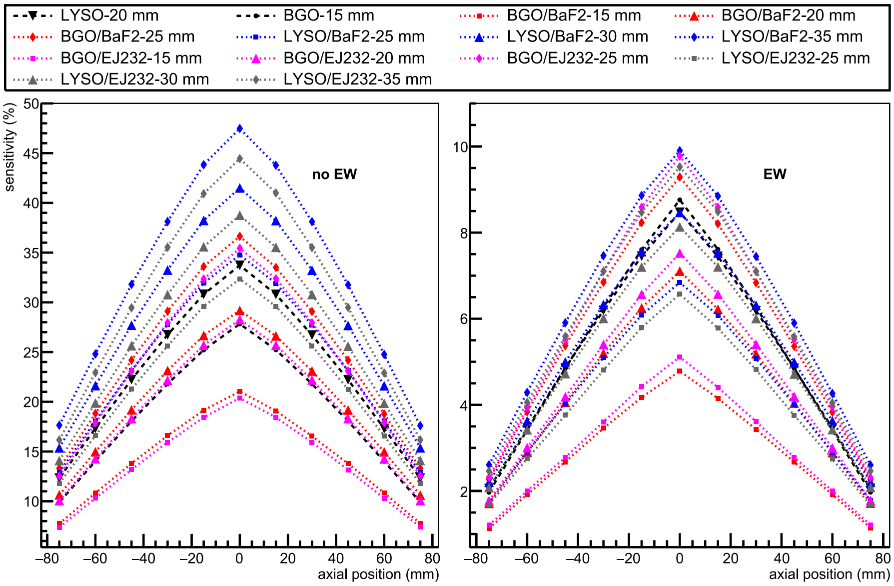

Fig. 5. Sensitivity profiles for ^{22}Na with and without energy window (EW). The black full circle represents a 15 mm thick bulk BGO, while the black downward triangle indicates a 20 mm thick bulk LYSO. The colors of the markers define the metascintillator materials: red for BGO/BaF2, blue for LYSO/BaF2, magenta for BGO/EJ232, and gray for LYSO/EJ232. Marker styles denote the thickness of the metascintillator based on its high-Z material: a full square indicates either 15 mm for BGO or 25 mm for LYSO; a full upward triangle represents 20 mm for BGO or 30 mm for LYSO; and a full diamond corresponds to 25 mm for BGO or 35 mm for LYSO. (For interpretation of the references to color in this figure legend, the reader is referred to the web version of this article.)

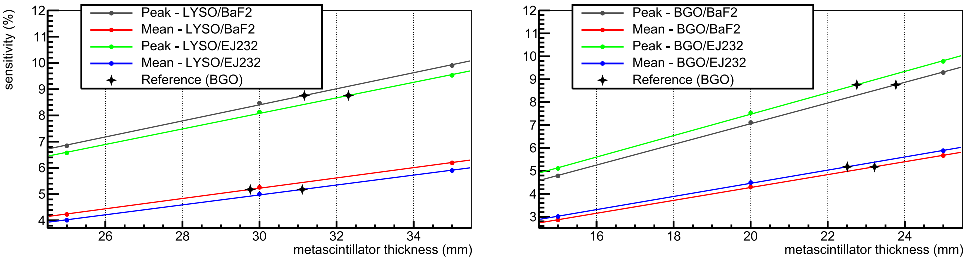

Fig. 6. Sensitivity as a functions of the BGO and LYSO-based metascintillators thicknesses with a 350–650 keV energy window. (For interpretation of the references to color in this figure legend, the reader is referred to the web version of this article.)

3.2. NECR and SF curves

Figs. 7 and 8 show the NECR and SF curves for the selected metascintillators with a thickness equivalent to a bulk BGO with 15 mm, considering the peak sensitivity as a worst case scenario. A 350–650 keV energy window was applied. Bulk BGO and LYSO were also included for comparison purposes.

Without ToF gain, scanners based on bulk LYSO and LYSO-EJ232 present the best NECR curves, reaching a peak of 130 cps at around 1600 MBq. This is due to the reduced dead time and pile up provided by the LYSO and EJ232 materials. On the other hand, BaF$_2$-based metascintillator systems provide the lowest NECR peak value due to the worst dead time/pile-up specifications.

With ToF gain applied according to Eq. (6), the scanner based on LYSO-EJ232 presents the best NECR curve. This is due to the enhanced timing properties provided by the LYSO and EJ232 materials. Bulk BGO-based scanner presents the NECR curve with the lowest values.

Concerning the SF curves, the lowest values are provided by the LYSO-EJ232-based scanner, followed by the system that uses the bulk LYSO crystal. The worst scenario is again represented by the BaF$_2$-based metascintillators scanners.

Table 6 summarizes the results in this work through the peak values of the sensitivity and NECR with and without ToF gain. Peak sensitivity ranges from 4.8% to 9.9%. The 25 mm LYSO/EJ232 scanner has the best peak NECR when receiving the boost from the ToF gain.

Table 6
Peak sensitivity (S) and NECR with and without the ToF SNR gain for each length (L). A is the activity of the obtained NECR value.

Scintillator	L (mm)	Peak S	ToF NECR gain	Peak NECR	Peak NECR ToF	A (MBq)
LYSO	20	8.5%	4.32	130	562	1600
BGO	15	8.8%	1.51	121	183	1150
BGO/BaF$_2$	15	4.8%	3.78	106	401	800
BGO/BaF$_2$	20	7.1%	3.72	106	394	800
BGO/BaF$_2$	23.7	8.8%	3.66	106	388	800
BGO/BaF$_2$	25	9.3%	3.64	106	386	800
BGO/EJ232	15	5.1%	4.43	118	522	1150
BGO/EJ232	20	7.5%	4.33	118	511	1150
BGO/EJ232	22.7	8.8%	4.27	118	503	1150
BGO/EJ232	25	9.8%	4.21	118	497	1150
LYSO/BaF$_2$	25	6.8%	9.08	106	962	800
LYSO/BaF$_2$	30	8.5%	7.94	106	842	800
LYSO/BaF$_2$	31.1	8.8%	7.72	106	819	800
LYSO/BaF$_2$	35	9.9%	7.03	106	745	800
LYSO/EJ232	25	6.6%	9.08	130	1180	1600
LYSO/EJ232	30	8.1%	7.94	130	1033	1600
LYSO/EJ232	32.3	8.8%	7.50	130	975	1600
LYSO/EJ232	35	9.5%	7.03	130	914	1600

Within the simulated scenarios, the best peak NECR with ToF is achieved by the 25 mm thick LYSO/EJ232 (1180 cps at 1600 MB), despite its lower peak sensitivity of 6.6%.

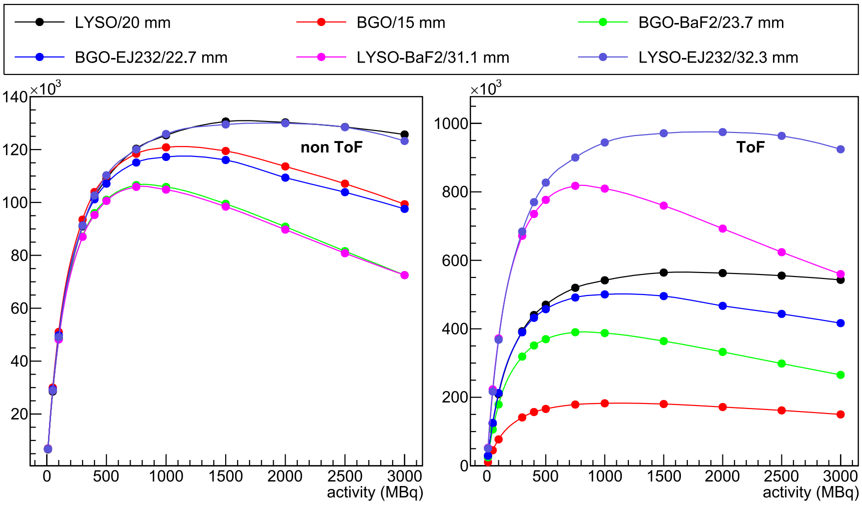

Fig. 7. NECR curves for ^{22}Na with and without ToF for the 350–650 keV energy window. (For interpretation of the references to color in this figure legend, the reader is referred to the web version of this article.)

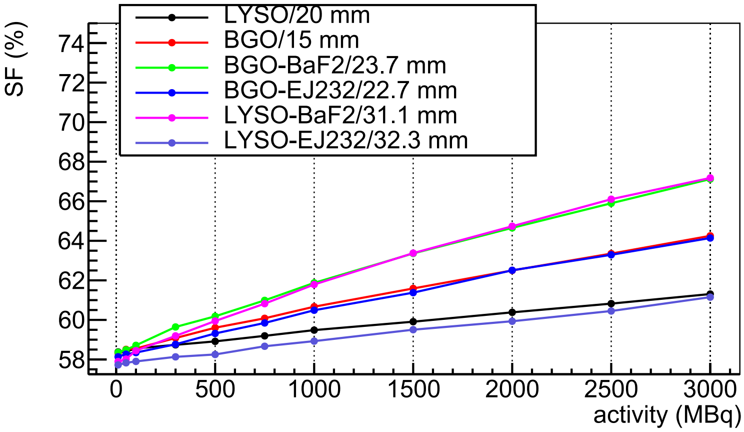

Fig. 8. SF curves for the 350–650 keV energy window. (For interpretation of the references to color in this figure legend, the reader is referred to the web version of this article.)

4. Discussion

The primary focus of applying metascintillators in PET lies in enhancing effective sensitivity through the use of ToF information, which can be analytically calculated to assess its impact on reconstructed images [69]. Studies have demonstrated that improved ToF capabilities pave the way for novel architectures, such as sparse or open configurations, while enhancing the ability to discriminate small lesions. Subsequent to this study, the simulated data will be utilized for image reconstruction of source distributions corresponding to real-world medical scenarios. Specifically, the target application involves a neurological study aimed at understanding the diffusion of amyloid plaques from white to gray matter in brains with normal activity and those afflicted by Alzheimer's disease. Such investigations stand to benefit from high-sensitivity PET systems with excellent ToF capabilities, as ToF information can mitigate noise propagation and enhance effective sensitivity.

Spatial resolution is an important aspect in brain PET systems, which was addressed by using small segmented crystal with one-to-one photosensor-crystal coupling readout. However, DOI significantly influences image quality, as parallax errors can degrade it. At the same time, DOI is a pivotal driver in ToF performance, potentially enhancing image quality and effective sensitivity. Consequently, DOI is the focus of metascintillator development, through the design of semi-monolithic metascintillators [70]. Further studies should explore the spatial resolution and image reconstruction algorithms.

The selected energy window ranges from 350 to 650 keV. A number of scattered events is thus registered by the system, albeit with low-energy deposition in the subject under study, resulting in slight deviations from the correct LOR. A study to optimize the energy window, focused on the experimentally retrieved energy resolution and photofractions is likely to improve the NECR curve.

The choice of materials for the metascintillator plays another vital role in the calculation of NECR, as the decay characteristics of different scintillators significantly affect the dead time of the detector. It is clear, in Fig. 7, that BaF_2-based solutions penalize NECR for higher activities. This can be amended by the use of yttrium-doped BaF_2, suppressing the slow part of the pulse and retaining the useful, ultra-fast, cross-luminescent component [71]. Moreover, BaF_2 timing has been based on an experiment using noncommercial Vacuum-ultraviolet (VUV) sensitive silicon photomultipliers (SiPMs), such as the one from Fundazione Bruno Kessler (FBK) [71]. Enhanced sensitivity in the VUV region can further improve timing with BaF_2. Combined with the suppression of the slow component, this material holds significant potential for future metascintillator applications.

The image noise can be reduced by increasing the number of total counts. Therefore, a longer acquisition time, a radiopharmaceutical with higher activity, and a more efficient detection system could improve the image noise. However, an increase in radiopharmaceutical activity is limited by the dead time of the system, the higher frequency of random coincidences and the absorbed dose in the patient. A longer acquisition time may be unfeasible/uncomfortable for a living organism or a patient. The efficiency of the detection system is also limited by the design of the tomograph. The image noise can be characterized by the NECR, as it is linearly proportional to the square of image signal-to-noise. Additionally, NECR and SF values exhibit a strong dependence on the size of the object under study, as well as the activity distribution and the parameters of the energy and timing windows. Hence, it is crucial to adhere to guidelines when comparing results with other studies.

Our design approach begins with single pixel experimental results, which are then used in simulations. Consequently, we compare our simulated metascintillator-based brain PET systems with those employing state-of-the-art crystals, such as 20 mm thick LYSO and 15 mm thick BGO. However, some works describe brain PET scanners with more segmented crystals and multi-layer configurations [72–74], which provide these systems with DOI capabilities, although their CTR values do not surpass the state-of-the-art.

The influence of metascintillator length on the CTR should be further assessed in future work, using experimental data to confirm or improve the assumptions of the model employed in this study.

Further enhancements in sensitivity and NECR can be achieved through the adoption of more intricate architectures, such as a jaw or neck detector array [75]. Notably, such architectures have not been combined with ToF and DOI, such as those that metascintillators are capable of including in the system. Exploring these avenues represents another promising direction for future development in this field.

5. Conclusion

Several metascintillator-based PET systems were simulated and compared against bulk LYSO and BGO-based scanners. Analyzed parameters were sensitivity, NECR and SF curves, adhering to NEMA guidelines [44]. GATE simulations of the sensitivity was previously evaluated with an analytical model [67]. For each metascintillator configuration, a specific thickness was determined to match its equivalence to a bulk BGO crystal in terms of sensitivity. Comparison procedures were based only in list-mode data to avoid dependence with image reconstruction algorithms.

To match the peak sensitivity of a PET system based on a 15 mm thick bulk BGO, the metascintillator-based scanners using BGO/BaF$_2$, BGO/EJ232, LYSO/BaF$_2$ and LYSO/EJ232 require thicknesses of 23.2 mm, 22.5 mm, 29.7 mm and 31.1 mm, respectively. This increase in length for sensitivity normalization slightly penalizes the timing characteristics of the system. However, fast emitters, such as the EJ232, retain favorable CTR values with extended lengths, owing to their brief scintillation pulse characteristics.

The scanner utilizing a 25 mm thick LYSO-EJ232 metascintillator exhibited the most promising NECR curve with ToF gain, peaking at 1180 cps at 1600 MBq.

Future work should follow NEMA guidelines, utilizing image reconstruction algorithms and estimating the point spread function with experimental data.

CRediT authorship contribution statement

D.A.B. Bonifacio: Writing – review & editing, Writing – original draft, Validation, Methodology, Investigation, Formal analysis, Conceptualization. **R. Latella:** Writing – review & editing, Methodology, Formal analysis, Conceptualization. **H.M. Murata:** Writing – review & editing, Visualization, Formal analysis. **J.M. Benlloch:** Writing – review & editing, Visualization, Project administration, Conceptualization. **A.J. Gonzalez:** Writing – review & editing, Visualization, Supervision, Methodology, Funding acquisition, Conceptualization. **P. Lecoq:** Writing – review & editing, Visualization, Supervision, Project administration, Methodology, Investigation, Funding acquisition, Formal analysis, Conceptualization. **G. Konstantinou:** Writing – review & editing, Writing – original draft, Validation, Supervision, Methodology, Investigation, Funding acquisition, Formal analysis, Conceptualization.

Declaration of competing interest

The authors declare that they have no known competing financial interests or personal relationships that could have appeared to influence the work reported in this paper.

Acknowledgments

This work has been initiated within the framework of a public–private partnership between the Multiwave Metacrystal SA company, based in Geneva (Switzerland), and the Instituto de Instrumentación para Imagen Molecular, Centro Mixto CSIC-UPV, 46022 Valencia (Spain). Their support is greatly acknowledged. Additionally, it has been in part supported by the European Research Council (ERC) under the European Union's Horizon 2020 research and innovation program (grant agreement No 695536): 4D-PET and the Brazilian funding agencies Conselho Nacional de Desenvolvimento Científico e Tecnológico (CNPq grant agreement No 202378/2020-9 and 435039/2018-0) and Financiadora de Estudos e Projetos, Brazil (FINEP grant agreement No 0294/16). The metascintillator concept presented in this manuscript was based on research first developed within the TICAL: 4D total absorptionTime Imaging CALorimeter ERC (grant agreement no 338953).

References

[1] S.R. Cherry, J.A. Sorenson, M.E. Phelps, Chapter 18 - positron emission tomography, in: S.R. Cherry, J.A. Sorenson, M.E. Phelps (Eds.), Physics in Nuclear Medicine (Fourth Edition), fourth ed., W.B. Saunders, Philadelphia, 2012, pp. 307–343, http://dx.doi.org/10.1016/B978-1-4160-5198-5.00018-6, URL https://www.sciencedirect.com/science/article/pii/B9781416051985000186.

[2] H. Li, R. Badawi, S. Cherry, K. Fontaine, L. He, L. Hu, T. Jones, E. Leung, T. Li, Y. Li, P. Liu, Z. Lu, S. Majewski, T. Mulnix, S. Samanta, A. Selfridge, X. Sun, J. Qi, R. Carson, Performance evaluation of a next-generation human brain PET imager: the NeuroEXPLORER, J. Nucl. Med. 64 (supplement 1) (2023) P801, arXiv:https://jnm.snmjournals.org/content, URL https://jnm.snmjournals.org/content/64/supplement_1/P801.

[3] X. Zeng, Z. Wang, W. Tan, E. Petersen, X. Cao, A. LaBella, A. Boccia, D. Franceschi, M. de Leon, G.C.-Y. Chiang, et al., A conformal TOF–DOI prism-PET prototype scanner for high-resolution quantitative neuroimaging, Med. Phys. 50 (6) (2023) 3401–3417.

[4] L. Caldeira, S. Lalitha, M. Lenz, R. Deepu, W. Klijn, C. Lerche, N. Shah, U. Pietrzyk, Full dynamic brain simulation using GATE in a high-performance computer, in: 2017 IEEE Nuclear Science Symposium and Medical Imaging Conference, NSS/MIC, IEEE, Atlanta, GA, 2017, pp. 1–3, http://dx.doi.org/10.1109/NSSMIC.2017.8532732, URL https://ieeexplore.ieee.org/document/8532732/.

[5] W. Tao, G. Chen, F. Weng, Y. Zan, Z. Zhao, Q. Peng, J. Xu, Q. Huang, Simulation study of a high-performance brain PET system with dodecahedral geometry, Med. Phys. 45 (7) (2018) 3297–3304, http://dx.doi.org/10.1002/mp.12996, URL https://onlinelibrary.wiley.com/doi/10.1002/mp.12996.

[6] J. Paredes-Pacheco, F.J. López-González, J. Silva-Rodríguez, N. Efthimiou, A. Niñerola-Baizán, A. Ruibal, N. Roé-Vellvé, P. Aguiar, SimPET—An open online platform for the Monte Carlo simulation of realistic brain PET data. Validation for ^{18} F-FDG scans, Med. Phys. 48 (5) (2021) 2482–2493, http://dx.doi.org/10.1002/mp.14838, URL https://onlinelibrary.wiley.com/doi/10.1002/mp.14838.

[7] B. Ma, H. Xu, M. Lenz, U. Pietrzyk, N.J. Shah, M. Gaens, L. Caldeira, J. Bert, P. Lohmann, L. Tellmann, C. Lerche, J. Scheins, E. Rota Kops, Scatter correction based on GPU-accelerated full Monte Carlo simulation for brain PET/MRI, IEEE Trans. Med. Imaging 39 (1) (2020) 140–151, http://dx.doi.org/10.1109/TMI.2019.2921872, URL https://ieeexplore.ieee.org/document/8733836/.

[8] E. Gaudin, M. Toussaint, C. Thibaudeau, M. Paille, R. Fontaine, R. Lecomte, Performance simulation of an ultrahigh resolution brain PET scanner using 1.2-mm pixel detectors, IEEE Trans. Radiat. Plasma Med. Sci. 3 (3) (2019) 334–342, http://dx.doi.org/10.1109/TRPMS.2018.2877511, URL https://ieeexplore.ieee.org/document/8502780/.

[9] L. Moliner, M.J. Rodríguez-Alvarez, J.V. Catret, A. González, V. Ilisie, J.M. Benlloch, NEMA Performance Evaluation of CareMiBrain dedicated brain PET and Comparison with the whole-body and dedicated brain PET systems, Sci. Rep. 9 (1) (2019) 15484, http://dx.doi.org/10.1038/s41598-019-51898-z, URL http://www.nature.com/articles/s41598-019-51898-z.

[10] S. Vandenberghe, E. Mikhaylova, E. D'Hoe, P. Mollet, J.S. Karp, Recent developments in time-of-flight PET, EJNMMI Phys. 3 (2016) 1–30.

[11] M. Weber, Scintillation: mechanisms and new crystals, Nucl. Instrum. Methods Phys. Res. A 527 (1–2) (2004) 9–14, http://dx.doi.org/10.1016/j.nima.2004.03.009, URL https://linkinghub.elsevier.com/retrieve/pii/S0168900204003559.

[12] Z. Lin, S. Lv, Z. Yang, J. Qiu, S. Zhou, Structured scintillators for efficient radiation detection, Adv. Sci. 9 (2) (2022) 2102439, http://dx.doi.org/10.1002/advs.202102439, URL https://onlinelibrary.wiley.com/doi/10.1002/advs.202102439.

[13] P. Lecoq, Development of new scintillators for medical applications, Nucl. Instrum. Methods Phys. Res. A 809 (2016) 130–139, http://dx.doi.org/10.1016/j.nima.2015.08.041, URL https://linkinghub.elsevier.com/retrieve/pii/S0168900215009754.

[14] S.I. Kwon, A. Gola, A. Ferri, C. Piemonte, S.R. Cherry, Bismuth germanate coupled to near ultraviolet silicon photomultipliers for time-of-flight PET, Phys. Med. Biol. 61 (18) (2016) L38, http://dx.doi.org/10.1088/0031-9155/61/18/L38.

[15] S. Brunner, D. Schaart, [BGO] as a hybrid scintillator/[c]herenkov radiator for cost-effective time-of-flight PET, Phys. Med. Biol. 62 (11) (2017) 4421.

[16] S. Gundacker, R.M. Turtos, E. Auffray, M. Paganoni, P. Lecoq, High-frequency SiPM readout advances measured coincidence time resolution limits in TOF-PET, Phys. Med. Biol. 64 (5) (2019) 055012.

[17] J.W. Cates, C.S. Levin, Electronics method to advance the coincidence time resolution with bismuth germanate, Phys. Med. Biol. 64 (17) (2019) 175016.

[18] S.I. Kwon, E. Roncali, A. Gola, G. Paternoster, C. Piemonte, S.R. Cherry, Dual-ended readout of bismuth germanate to improve timing resolution in time-of-flight PET, Phys. Med. Biol. 64 (10) (2019) 105007.

[19] E. Roncali, S.I. Kwon, S. Jan, E. Berg, S.R. Cherry, Cerenkov light transport in scintillation crystals explained: realistic simulation with GATE, Biomed. Phys. Eng. Expr. 5 (3) (2019) 035033.

[20] N. Kratochwil, S. Gundacker, P. Lecoq, E. Auffray, Pushing Cherenkov PET with BGO via coincidence time resolution classification and correction, Phys. Med. Biol. 65 (11) (2020) 115004.

[21] J. Du, G. Ariño-Estrada, X. Bai, S.R. Cherry, Performance comparison of dual-ended readout depth-encoding PET detectors based on BGO and LYSO crystals, Phys. Med. Biol. 65 (23) (2020) 235030.

[22] N. Efthimiou, N. Kratochwil, S. Gundacker, A. Polesel, M. Salomoni, E. Auffray, M. Pizzichemi, TOF-pet image reconstruction with multiple timing kernels applied on cherenkov radiation in BGO, IEEE Trans. Radiation Plasma Med. Sci. 5 (5) (2020) 703–711.

[23] S. Gundacker, R.M. Turtos, N. Kratochwil, R.H. Pots, M. Paganoni, P. Lecoq, E. Auffray, Experimental time resolution limits of modern SiPMs and TOF-PET detectors exploring different scintillators and cherenkov emission, Phys. Med. Biol. 65 (2) (2020) 025001.

[24] N. Kratochwil, S. Gundacker, E. Auffray, A roadmap for sole cherenkov radiators with SiPMs in TOF-PET, Phys. Med. Biol. 66 (19) (2021) 195001.

[25] J.W. Cates, W.-S. Choong, Low power implementation of high frequency SiPM readout for Cherenkov and scintillation detectors in TOF-PET, Phys. Med. Biol. 67 (19) (2022) 195009.

[26] M. Krake, V. Nadig, V. Schulz, S. Gundacker, Power-efficient high-frequency readout concepts of SiPMs for TOF-PET and HEP, Nucl. Instrum. Methods Phys. Res. A 1039 (2022) 167032.

[27] A. Gonzalez-Montoro, S. Pourashraf, J.W. Cates, C.S. Levin, Study of novel photodetectors and electronics to enhance coincidence time resolution of BGO-based PET detectors, in: 2022 IEEE Nuclear Science Symposium and Medical Imaging Conference, NSS/MIC, IEEE, 2022, pp. 1–3.

[28] P. Krause, E. Rogers, M.D. Birowosuto, Q. Pei, E. Auffray, A.N. Vasil'ev, G. Bizarri, Design rules for time of flight positron emission tomography (tof-PET) heterostructure radiation detectors, Heliyon 8 (6) (2022) e09754.

[29] F. Loignon-Houle, M. Toussaint, E. Bertrand, F.C. Lemyre, R. Lecomte, Timing estimation and limits in TOF-PET detectors producing prompt photons, IEEE Trans. Radiat. Plasma Med. Sci. 7 (7) (2023) 692–703.

[30] S. Gundacker, G. Borghi, S.R. Cherry, A. Gola, D. Lee, S. Merzi, M. Penna, V. Schulz, S.I. Kwon, On timing-optimized SiPMs for cherenkov detection to boost low cost time-of-flight PET, Phys. Med. Biol. 68 (16) (2023) 165016.

[31] D.R. Schaart, S. Seifert, R. Vinke, H.T. van Dam, P. Dendooven, H. Löhner, F.J. Beekman, LaBr3: Ce and SiPMs for time-of-flight PET: achieving 100 ps coincidence resolving time, Phys. Med. Biol. 55 (7) (2010) N179.

[32] P. Kowalski, W. Wiślicki, R.Y. Shopa, L. Raczyński, K. Klimaszewski, C. Curcenau, E. Czerwiński, K. Dulski, A. Gajos, M. Gorgol, et al., Estimating the NEMA characteristics of the J-PET tomograph using the GATE package, Phys. Med. Biol. 63 (16) (2018) 165008.

[33] R.M. Turtos, S. Gundacker, E. Auffray, P. Lecoq, Towards a metamaterial approach for fast timing in PET: experimental proof-of-concept, Phys. Med. Biol. 64 (18) (2019) 185018, http://dx.doi.org/10.1088/1361-6560/ab18b3.

[34] G. Konstantinou, P. Lecoq, J.M. Benlloch, A.J. Gonzalez, Metascintillators for ultrafast Gamma detectors: A review of current state and future perspectives, IEEE Trans. Radiat. Plasma Med. Sci. 6 (1) (2022) 5–15, http://dx.doi.org/10.1109/TRPMS.2021.3069624, URL https://ieeexplore.ieee.org/document/9394412/.

[35] P. Lecoq, G. Konstantinou, R. Latella, L. Moliner, J. Nuyts, L. Zhang, J. Barrio, J.M. Benlloch, A.J. Gonzalez, Metascintillators: New results for TOFPET applications, IEEE Trans. Radiat. Plasma Med. Sci. (2022) 1, http://dx.doi.org/10.1109/TRPMS.2022.3161473, URL https://ieeexplore.ieee.org/document/9740339/.

[36] F. Pagano, N. Kratochwil, M. Salomoni, M. Pizzichemi, M. Paganoni, E. Auffray, Advances in heterostructured scintillators: toward a new generation of detectors for TOF-PET, Phys. Med. Biol. 67 (13) (2022) 135010, http://dx.doi.org/10.1088/1361-6560/ac72ee.

[37] E.G. Rogers, M.D. Birowosuto, F. Maddalena, C. Dujardin, F. Pagano, N. Kratochwil, E. Auffray, P. Krause, G. Bizarri, Two-dimensional perovskite functionalized fiber-type heterostructured scintillators, Appl. Phys. Lett. 122 (8) (2023) 081901.

[38] F. Loignon-Houle, S.A. Charlebois, R. Fontaine, R. Lecomte, Monte Carlo simulations of energy, time and spatial evolution of primary electrons generated by 511 keV photons in various scintillators, Nucl. Instrum. Methods Phys. Res. A 1030 (2022) 166449, http://dx.doi.org/10.1016/j.nima.2022.166449, URL https://linkinghub.elsevier.com/retrieve/pii/S0168900222000912.

[39] D. Sarrut, M. Bała, M. Bardiès, J. Bert, M. Chauvin, K. Chatzipapas, M. Dupont, A. Etxebeste, L. M Fanchon, S. Jan, G. Kayal, A. S. Kirov, P. Kowalski, W. Krzemien, J. Labour, M. Lenz, G. Loudos, B. Mehadji, L. Ménard, C. Morel, P. Papadimitroulas, M. Rafecas, J. Salvadori, D. Seiter, M. Stockhoff, E. Testa, C. Trigila, U. Pietrzyk, S. Vandenberghe, M.-A. Verdier, D. Visvikis, K. Ziemons, M. Zvolský, E. Roncali, Advanced Monte Carlo simulations of emission tomography imaging systems with GATE, Phys. Med. Biol. 66 (10) (2021) 10TR03, http://dx.doi.org/10.1088/1361-6560/abf276, URL https://iopscience.iop.org/article/10.1088/1361-6560/abf276.

[40] J. Salvadori, J. Labour, F. Odille, P.-Y. Marie, J.-N. Badel, L. Imbert, D. Sarrut, Monte Carlo simulation of digital photon counting PET, EJNMMI Phys. 7 (1) (2020) 23, http://dx.doi.org/10.1186/s40658-020-00288-w, URL https://ejnmmiphys.springeropen.com/articles/10.1186/s40658-020-00288-w.

[41] S. Jan, G. Santin, D. Strul, S. Staelens, K. Assié, D. Autret, S. Avner, R. Barbier, M. Bardiès, P.M. Bloomfield, D. Brasse, V. Breton, P. Bruyndonckx, I. Buvat, A.F. Chatziioannou, Y. Choi, Y.H. Chung, C. Comtat, D. Donnarieix, L. Ferrer, S.J. Glick, C.J. Groiselle, D. Guez, P.-F. Honore, S. Kerhoas-Cavata, A.S. Kirov, V. Kohli, M. Koole, M. Krieguer, D.J.v. Laan, F. Lamare, G. Largeron, C. Lartizien, D. Lazaro, M.C. Maas, L. Maigne, F. Mayet, F. Melot, C. Merheb, E. Pennacchio, J. Perez, U. Pietrzyk, F.R. Rannou, M. Rey, D.R. Schaart, C.R. Schmidtlein, L. Simon, T.Y. Song, J.-M. Vieira, D. Visvikis, R.V. Walle, E. Wieërs, C. Morel, GATE: a simulation toolkit for PET and SPECT, Phys. Med. Biol. 49 (19) (2004) 4543–4561, http://dx.doi.org/10.1088/0031-9155/49/19/007, URL https://iopscience.iop.org/article/10.1088/0031-9155/49/19/007.

[42] S. Agostinelli, J. Allison, K. Amako, J. Apostolakis, H. Araujo, P. Arce, M. Asai, D. Axen, S. Banerjee, G. Barrand, F. Behner, L. Bellagamba, J. Boudreau, L. Broglia, A. Brunengo, H. Burkhardt, S. Chauvie, J. Chuma, R. Chytracek, G. Cooperman, G. Cosmo, P. Degtyarenko, A. Dell'Acqua, G. Depaola, D. Dietrich, R. Enami, A. Feliciello, C. Ferguson, H. Fesefeldt, G. Folger, F. Foppiano, A. Forti, S. Garelli, S. Giani, R. Giannitrapani, D. Gibin, J.J. Gómez Cadenas, I. González, G. Gracia Abril, G. Greeniaus, W. Greiner, V. Grichine, A. Grossheim, S. Guatelli, P. Gumplinger, R. Hamatsu, K. Hashimoto, H. Hasui, A. Heikkinen, A. Howard, V. Ivanchenko, A. Johnson, F.W. Jones, J. Kallenbach, N. Kanaya, M. Kawabata, Y. Kawabata, M. Kawaguti, S. Kelner, P. Kent, A. Kimura, T. Kodama, R. Kokoulin, M. Kossov, H. Kurashige, E. Lamanna, T. Lampén, V. Lara, V. Lefebure, F. Lei, M. Liendl, W. Lockman, F. Longo, S. Magni, M. Maire, E. Medernach, K. Minamimoto, P. Mora de Freitas, Y. Morita, K. Murakami, M. Nagamatu, R. Nartallo, P. Nieminen, T. Nishimura, K. Ohtsubo, M. Okamura, S. O'Neale, Y. Oohata, K. Paech, J. Perl, A. Pfeiffer, M.G. Pia, F. Ranjard, A. Rybin, S. Sadilov, E. Di Salvo, G. Santin, T. Sasaki, N. Savvas, Y. Sawada, S. Scherer, S. Sei, V. Sirotenko, D. Smith, N. Starkov, H. Stoecker, J. Sulkimo, M. Takahata, S. Tanaka, E. Tcherniaev, E. Safai Tehrani, M. Tropeano, P. Truscott, H. Uno, L. Urban, P. Urban, M. Verderi, A. Walkden, W. Wander, H. Weber, J.P. Wellisch, T. Wenaus, D.C. Williams, D. Wright, T. Yamada, H. Yoshida, D. Zschiesche, G4–a simulation toolkit, Nucl. Instrum. Methods Phys. Res. A 506 (3) (2003) 250–303, http://dx.doi.org/10.1016/S0168-9002(03)01368-8, URL http://www.sciencedirect.com/science/article/B6TJM-48TJFY8-5/2/23ea98096ce11c1be446850c04cfa498.

[43] P. Mohr, N. Efthimiou, F. Pagano, N. Kratochwil, M. Pizzichemi, C. Tsoumpas, E. Auffray, K. Ziemons, Image reconstruction analysis for positron emission tomography with heterostructured scintillators, IEEE Trans. Radiat. Plasma Med. Sci. 7 (1) (2023) 41–51.

[44] NEMA, NU 4-2008. performance measurements of small animal positron emission tomographs, 2008.

[45] NEMA, NEMA standards publication NU 2-2018: Performance measurements of positron emission tomographs, in: NEMA standards publication, National Electrical Manufacturers Association, 2018.

[46] C. Catana, Development of dedicated brain PET imaging devices: Recent advances and future perspectives, J. Nucl. Med. 60 (8) (2019) 1044–1052, http://dx.doi.org/10.2967/jnumed.118.217901, arXiv:https://jnm.snmjournals.org/content/60/8/1044.full.pdf, URL https://jnm.snmjournals.org/content/60/8/1044.

[47] LYSO Scintillation Crystals | Crystals, URL https://www.crystals.saint-gobain.com/radiation-detection-scintillators/crystal-scintillators/lyso-scintillation-crystals.

[48] R.H. Pots, E. Auffray, S. Gundacker, Exploiting cross-luminescence in BaF2 for ultrafast timing applications using deep-ultraviolet sensitive HPK silicon photomultipliers, Front. Phys. 8 (2020) 592875, http://dx.doi.org/10.3389/fphy.2020.592875, URL https://www.frontiersin.org/articles/10.3389/fphy.2020.592875/full.

[49] EJ-232, EJ-232Q - Fast Timing Plastic Scintillator - Eljen Technology, URL https://eljentechnology.com/products/plastic-scintillators/ej-232-ej-232q.

[50] S. Seltzer, XCOM-Photon Cross Sections Database, NIST Standard Reference Database 8, 1987, http://dx.doi.org/10.18434/T48G6X, Type: dataset, URL http://www.nist.gov/pml/data/xcom/index.cfm.

[51] G. Konstantinou, R. Latella, L. Moliner, L. Zhang, J.M. Benlloch, A.J. Gonzalez, P. Lecoq, A proof-of-concept of cross-luminescent metascintillators: testing results on a BGO:BaF2 metapixel, Phys. Med. Biol. 68 (2) (2023) 025018.

[52] P. Arce, D. Bolst, M.-C. Bordage, J.M.C. Brown, P. Cirrone, M.A. Cortés-Giraldo, D. Cutajar, G. Cuttone, L. Desorgher, P. Dondero, A. Dotti, B. Faddegon, C. Fedon, S. Guatelli, S. Incerti, V. Ivanchenko, D. Konstantinov, I. Kyriakou, G. Latyshev, A. Le, C. Mancini-Terracciano, M. Maire, A. Mantero, M. Novak, C. Omachi, L. Pandola, A. Perales, Y. Perrot, G. Petringa, J.M. Quesada, J. Ramos-Méndez, F. Romano, A.B. Rosenfeld, L.G. Sarmiento, D. Sakata, T. Sasaki, I. Sechopoulos, E.C. Simpson, T. Toshito, D.H. Wright, Report on G4-Med, a Geant4 benchmarking system for medical physics applications developed by the Geant4 medical simulation benchmarking group, Med. Phys. 48 (1) (2021) 19–56, http://dx.doi.org/10.1002/mp.14226, URL https://onlinelibrary.wiley.com/doi/10.1002/mp.14226.

[53] Z. Li, C. Michelet, S. Incerti, V. Ivanchenko, M. Novak, S. Guatelli, H. Seznec, Implementation of the EPICS2017 database for photons in Geant4, Phys. Medica 95 (2022) 94–115, http://dx.doi.org/10.1016/j.ejmp.2022.01.008, URL https://linkinghub.elsevier.com/retrieve/pii/S1120179722014090.

[54] P. Kowalski, W. Wiślicki, R.Y. Shopa, L. Raczyński, K. Klimaszewski, C. Curcenau, E. Czerwiński, K. Dulski, A. Gajos, M. Gorgol, N. Gupta-Sharma, B. Hiesmayr, B. Jasińska, L. Kapł on, D. Kisielewska-Kamińska, G. Korcyl, T. Kozik, W. Krzemień, E. Kubicz, M. Mohammed, S. Niedźwiecki, M. Pałka, M. Pawlik-Niedźwiecka, J. Raj, K. Rakoczy, Z. Rudy, S. Sharma, S. Shivani, M. Silarski, M. Skurzok, B. Zgardzińska, M. Zieliński, P. Moskal, Estimating the NEMA characteristics of the J-PET tomograph using the GATE package, Phys. Med. Biol. 63 (16) (2018) 165008, http://dx.doi.org/10.1088/1361-6560/aad29b, URL https://iopscience.iop.org/article/10.1088/1361-6560/aad29b.

[55] R. Brun, F. Rademakers, ROOT — An object oriented data analysis framework, Nucl. Instrum. Methods Phys. Res. A 389 (1–2) (1997) 81–86, http://dx.doi.org/10.1016/S0168-9002(97)00048-X, URL https://linkinghub.elsevier.com/retrieve/pii/S016890029700048X.

[56] G. Konstantinou, R. Latella, L. Moliner, L. Zhang, J. Benlloch, A. Gonzalez, P. Lecoq, Metascintillator pulse feature and shape analysis to detect photoelectric interactions and energy sharing, in: 2020 IEEE Nuclear Science Symposium and Medical Imaging Conference, NSS/MIC, 2021, pp. 1–4.

[57] J. van Sluis, J. de Jong, J. Schaar, W. Noordzij, P. van Snick, R. Dierckx, R. Borra, A. Willemsen, R. Boellaard, Performance characteristics of the digital iograph vision PET/CT system, J. Nucl. Med. 60 (7) (2019) 1031–1036, http://dx.doi.org/10.2967/jnumed.118.215418, URL http://jnm.snmjournals.org/lookup/doi/10.2967/jnumed.118.215418.

[58] N. Efthimiou, E. Emond, P. Wadhwa, C. Cawthorne, C. Tsoumpas, K. Thielemans, Implementation and validation of time-of-flight PET image reconstruction module for listmode and sinogram projection data in the stir library, Phys. Med. Biol. 64 (3) (2019) 035004, http://dx.doi.org/10.1088/1361-6560/aaf9b9.

[59] E. Yoshida, H. Tashima, G. Akamatsu, Y. Iwao, M. Takahashi, T. Yamashita, T. Yamaya, 245 ps-TOF brain-dedicated PET prototype with a hemispherical detector arrangement, Phys. Med. Biol. 65 (14) (2020) 145008, http://dx.doi.org/10.1088/1361-6560/ab8c91, URL https://iopscience.iop.org/article/10.1088/1361-6560/ab8c91.

[60] Y. Onishi, T. Isobe, M. Ito, F. Hashimoto, T. Omura, E. Yoshikawa, Performance evaluation of dedicated brain PET scanner with motion correction system, Ann. Nucl. Med. 36 (8) (2022) 746–755, http://dx.doi.org/10.1007/s12149-022-01757-1, URL https://link.springer.com/10.1007/s12149-022-01757-1.

[61] A. Merlet, B. Presles, K.-H. Su, J. Salvadori, F. Sayah, H. Jozi, A. Cochet, J.-M. Vrigneaud, Validation of a discovery MI 4-ring model according to the NEMA nu 2-2018 standards: from Monte Carlo simulations to clinical-like reconstructions, EJNMMI Phys. 11 (1) (2024) 13.

[62] J. Strydhorst, I. Buvat, Redesign of the GATE PET coincidence sorter, Phys. Med. Biol. 61 (18) (2016) N522–N531, http://dx.doi.org/10.1088/0031-9155/61/18/N522, URL https://iopscience.iop.org/article/10.1088/0031-9155/61/18/N522.

[63] D.A.B. Bonifacio, N. Belcari, S. Moehrs, M. Moralles, V. Rosso, S. Vecchio, A. Del Guerra, A time efficient optical model for GATE simulation of a LYSO scintillation matrix used in PET applications, IEEE Trans. Nucl. Sci. 57 (5) (2010) 2483–2489, http://dx.doi.org/10.1109/TNS.2010.2062536, URL http://ieeexplore.ieee.org/document/5571048/.

[64] M. Conti, B. Bendriem, The new opportunities for high time resolution clinical TOF PET, Clinical Translat. Imaging 7 (2) (2019) 139–147.

[65] M. Conti, L. Eriksson, V. Westerwoudt, Estimating image quality for future generations of TOF PET scanners, IEEE Trans. Nucl. Sci. 60 (1) (2013) 87–94, http://dx.doi.org/10.1109/TNS.2012.2233214.

[66] J.P. Schmall, J.S. Karp, M. Werner, S. Surti, Parallax error in long-axial field-of-view PET scanners—a simulation study, Phys. Med. Biol. 61 (14) (2016) 5443.

[67] D.A.B. Bonifacio, R. Latella, H.M. Murata, J.M. Benlloch, A. Gonzalez, P. LECOQ, G. Konstantinou, Analytical modeling of the sensitivity of cylindrical PET systems based on bulk materials and metascintillators, 2023, http://dx.doi.org/10.36227/techrxiv.22637731.v1, Authorea Preprints.

[68] S. Surti, M.E. Werner, J.S. Karp, Study of PET scanner designs using clinical metrics to optimize the scanner axial FOV and crystal thickness, Phys. Med. Biol. 58 (12) (2013) 3995, http://dx.doi.org/10.1088/0031-9155/58/12/3995.

[69] M. Conti, Focus on time-of-flight PET: the benefits of improved time resolution, Eur. J. Nuclear Med. Molecular Imaging 38 (6) (2011) 1147–1157.

[70] G. Konstantinou, L. Zhang, A. Gonzalez, P. LECOQ, Semi-monolithic meta-scintillator simulation proof-of-concept, combining accurate DOI and TOF, 2023, Authorea Preprints.

[71] K. Herweg, V. Nadig, V. Schulz, S. Gundacker, On the prospects of BaF2 as a fast scintillator for time-of-flight positron emission tomography systems, IEEE Trans. Radiat. Plasma Med. Sci. 7 (3) (2023) 241–252.

[72] E. Yoshida, H. Tashima, G. Akamatsu, Y. Iwao, M. Takahashi, T. Yamashita, T. Yamaya, 245 ps-TOF brain-dedicated PET prototype with a hemispherical detector arrangement, Phys. Med. Biol. 65 (14) (2020) 145008, http://dx.doi.org/10.1088/1361-6560/ab8c91.

[73] W. He, Y. Zhao, W. Huang, X. Zhao, M. Niu, H. Yang, L. Zhang, Q. Ren, Z. Gu, A multi-resolution TOF-DOI detector for human brain dedicated pet scanner, Phys. Med. Biol. 69 (2) (2024) 025023, http://dx.doi.org/10.1088/1361-6560/ad1b6b.

[74] M. Watanabe, A. Saito, T. Isobe, K. Ote, R. Yamada, T. Moriya, T. Omura, Performance evaluation of a high-resolution brain PET scanner using four-layer MPPC DOI detectors, Phys. Med. Biol. 62 (17) (2017) 7148, http://dx.doi.org/10.1088/1361-6560/aa82e8.

[75] G. Akamatsu, M. Takahashi, H. Tashima, Y. Iwao, E. Yoshida, H. Wakizaka, M. Kumagai, T. Yamashita, T. Yamaya, Performance evaluation of VRAIN: a brain-dedicated PET with a hemispherical detector arrangement, Phys. Med. Biol. 67 (22) (2022) 225011.